nature physics

Article

https://doi.org/10.1038/s41567-024-02487-z

Spin Berry curvature-enhanced orbital Zeeman effect in a kagome metal

In the format provided by the authors and unedited

Supplementary Information

Supplementary Note 1. Discussion of the role of Tb magnetic moments in the observed band structure change

In this section, we explain in detail why: (1) there *must be* substantial contributions beyond Tb moments enhanced by exchange interactions to explain our observations, and (2) the effects from Tb magnetic moments are likely minimal in our system.

First, we observe no change in the electronic density of states as the system enters from the paramagnetic to the ferromagnetic state (Extended Data Figure 1, Figure 2a). This is in contrast to the kagome ferromagnets (kagome net formed by magnetic atoms of Fe, Co or Mn) where band structure changes tremendously as the system enters the ferromagnetic phase.

In principle, as the spins are aligned with external magnetic field, one could expect Tb magnetic moments and exchange interaction to affect the electronic bands, resulting in a continuous evolution. However, once all spins are fully aligned, applying additional magnetic field would lead to a minimal change, driven by the tiny conventional spin *g*-factor. This is what happens in the canonical case of Fe_3Sn_2, also a ferromagnet but with strongly spin-polarized low-energy kagome Fe *d* bands, where band structure change ceases to evolve exactly concomitant with the magnetization saturation [1,2]. If this scenario was at the root of our observations, we would expect a noticeable discontinuity of band evolution measured by STM after the Tb magnetic moment saturation is reached. However, we do not observe any anomalies in the dispersion of band features measured by STM when magnetization saturation is reached (Supplementary Figure 1).

Magnetization saturation will be somewhat temperature dependent. Therefore, we perform extensive comparison between the evolution of our STM data and bulk magnetization as a function of temperature (Supplementary Figure 1). In all cases, electronic band structure evolves well past the point when Tb magnetic moments are fully aligned out-of-plane. For example, at 2 K, band structure evolution extracted from STM continues to about 2 T, which is four times the value of magnetization saturation field H_c ~ 0.5 T at that same temperature; at 4 K and about 0.5 T, bulk magnetization is ~90% of its maximum value while the energy shift measured by STM only reached ~20% of its ultimate value. From this we can conclude that the majority of the electronic band shift must come from factors other than Tb spin magnetic moment alignment and spin exchange physics. Berry curvature driven orbital magnetic moments m(*k*) present a concrete theoretical explanation for this regime, which nicely explains the enormous magnitude of the effect.

Having established the contributions from m(k) for $H > H_c$, it is important to note that m(k) will also contribute to band shift for $H < H_c$ (non-zero m(k) emerges even in zero field due to spin-orbit coupling). Extrapolating the rate of change dE^*/dB just above H_c to fields less than H_c, one can see that the majority of the shift can be accounted for. From this we conclude that only a small portion of the electronic band shift at the order of a few meV may possibly come from Tb spin contributions via an exchange interaction, but that the majority of the observed band shift arises from the Berry curvature induced m(k).

Supplementary Note 2. Qualitative understanding of the *g* factor at *k*=0

We consider a well-known low-energy expansion of the kagome Hamiltonian with spin orbit coupling (SOC) λ near the Dirac point [3]:

$$h_k = v(\tau_3 k_x + \tau_1 k_y) + \tau_2 \frac{\Delta}{2}$$

Where $v = 2\sqrt{3}t$ is the Fermi velocity, τ_i $(i = 1, 2, 3)$ are Pauli matrices, and $\Delta = 4\sqrt{3}\lambda$ is the SOC gap.

By applying this low-energy effective Hamiltonian to the modern orbital magnetization formula (2):

$$m_n(k) = -i\frac{e}{2\hbar}\langle\nabla_k n| \times [h_k - \varepsilon_{nk}]|\nabla_k n\rangle$$

where $|n\rangle$ is the nth eigenvector and ε_{nk} is the nth eigenvalue of the Hamiltonian, with its gauge invariant form:

$$m_n(k) = u_B \frac{m_e}{\hbar^2} \sum_{n' \neq n} \frac{2\langle n|\partial_{kx} h_k|n'\rangle\langle n'|\partial_{ky} h_k|n\rangle}{\varepsilon_n - \varepsilon_{n'}}$$

we are able to get an analytical expression for the *k*-dependent orbital magnetization magnitude near the Dirac point as:

$$m(k) = u_B \frac{m_e}{\hbar^2} \frac{v^2\Delta}{4k^2v^2 + \Delta^2}$$

where $m_e = 9.1 \times 10^{-31} kg$. As it can be seen, *m*(*k*) peaks at *k* = 0, which is consistent with what has been observed here in TbV_6Sn_6. Using the conversion $-\frac{1}{2} g_k u_B \cdot B = -m_k \cdot B$, then the effective *g* factor at *k* = 0 can be written as:

$$g_{k=0} = \frac{4m_e}{\hbar^2} \frac{v^2}{\Delta}$$

As a result, the maximum *g* factor is proportional to the square of the Dirac band velocity and inversely proportional to the Dirac gap size. This may provide a potential guiding principle to create solids with larger unconventional magnetic moments, by maximizing the Dirac velocity and generating a small, yet finite SOC-induced gap.

Supplementary References

1. Yin, J.-X. X. *et al.* Giant and anisotropic many-body spin–orbit tunability in a strongly correlated kagome magnet. *Nature* **562**, 91–95 (2018).
2. Ren, Z. *et al.* Plethora of tunable Weyl fermions in kagome magnet Fe_3Sn_2 thin films. *npj Quantum Mater.* **7**, 109 (2022).
3. Guo, H.-M. & Franz, M. Topological insulator on the kagome lattice. *Phys. Rev. B* 80, 113102 (2009).

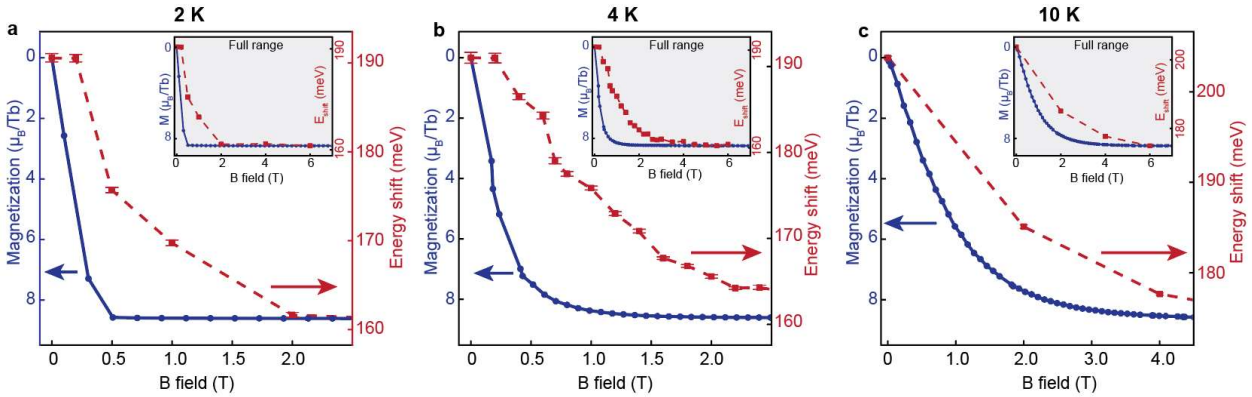

Supplementary Figure 1. Comparison between bulk magnetization data and the evolution of electronic band features from STM data as a function of temperature. Blue data points and lines represent bulk magnetization data taken at (a) 2 K, (b) 4 K and (c) 10 K respectively with magnetic field applied perpendicular to the sample surface. Red data points and dashed lines represent the positions of spectral features ($E^* \pm \delta E^*$) seen in STM dI/dV spectra in Figure 2 at those same temperatures. The insets at each temperature display the same data in a full magnetic field range up to 7 T. The error bar δE^* represents standard error of peak position in energy axis from Gaussian peak fittings of dI^3/dV^3 curve (number of data points for each curve is 126). STM setup conditions: I_{set} = 1 nA, V_{sample} = 300 mV, V_{exc} = 2 mV (2 K, 4 K); I_{set} = 500 pA, V_{sample} = 300 mV, V_{exc} = 2 mV (10 K).

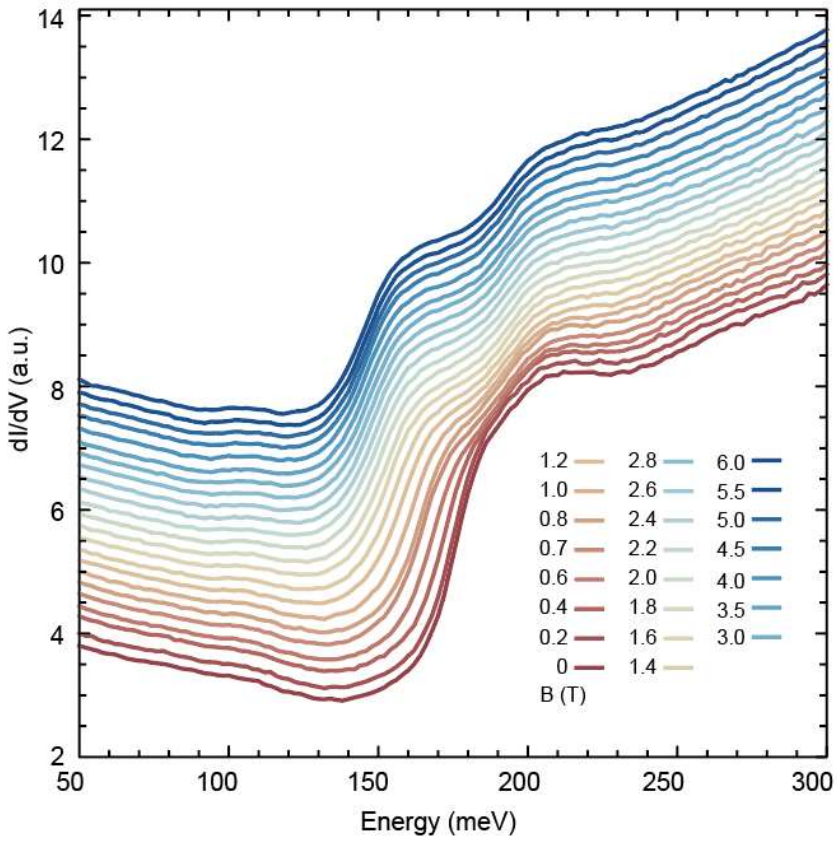

Supplementary Figure 2. Waterfall plot of dI/dV spectra shown in main Figure 2(b).

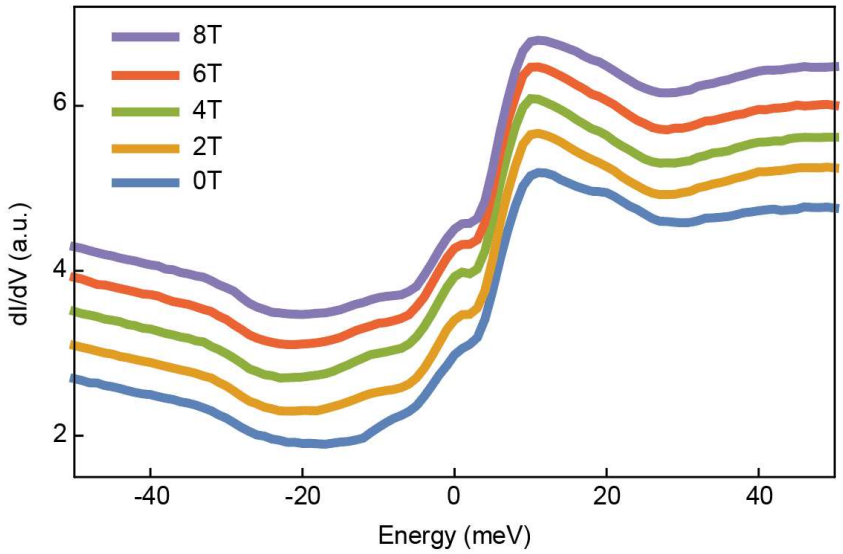

Supplementary Figure 3. The waterfall plot of dI/dV spectra acquired at an energy range near Fermi level as a function of magnetic field applied perpendicular to the sample surface. STM setup condition: I_{set} = 300 pA, V_{sample} = 50 mV, V_{exc} = 1 mV. Measurement temperature was 4.2 K.

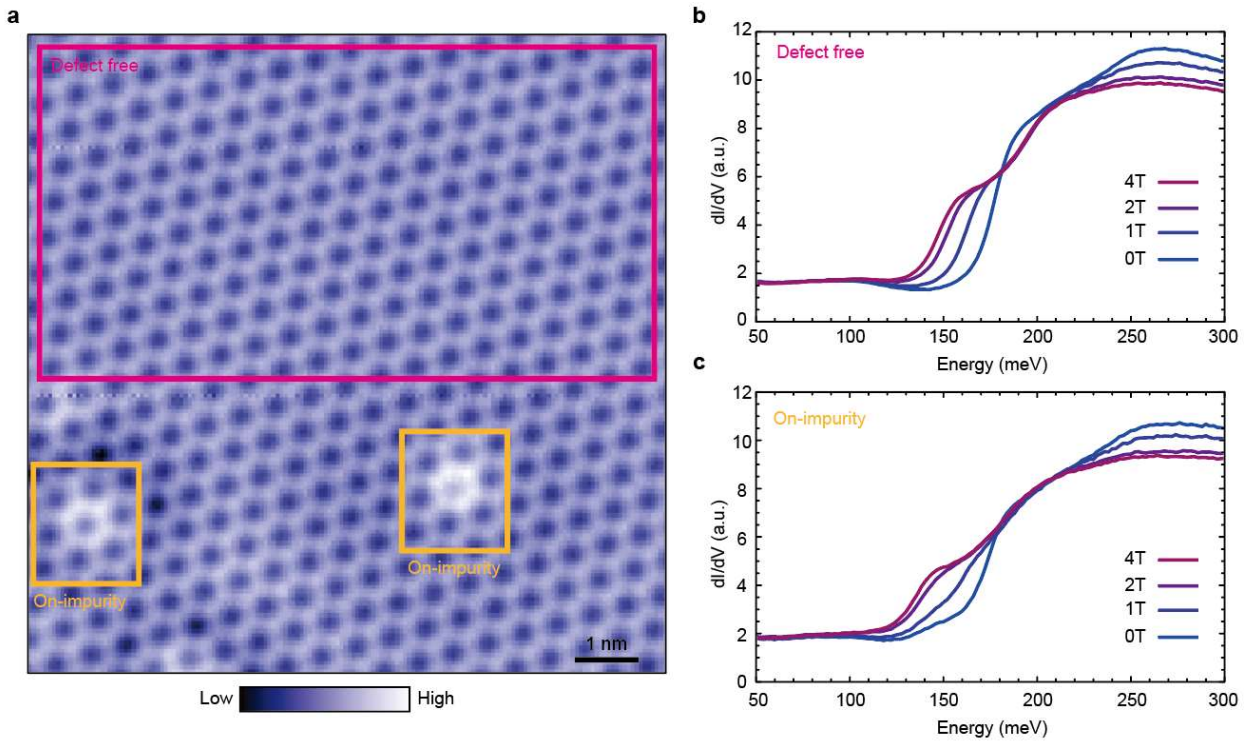

Supplementary Figure 4. (a) STM topograph of the Sn^2 surface. Average dI/dV spectra as a function of magnetic field applied perpendicular to the sample surface in: (b) defect free region enclosed by the pink rectangle in (a), and (c) on top of impurity regions enclosed by the two orange squares in (a). STM setup condition: I_{set} = 1 nA, V_{sample} = 300 mV (a); I_{set} = 1 nA, V_{sample} = 300 mV, V_{exc} = 2 mV (b,c). Measurement temperature was 4.2 K.

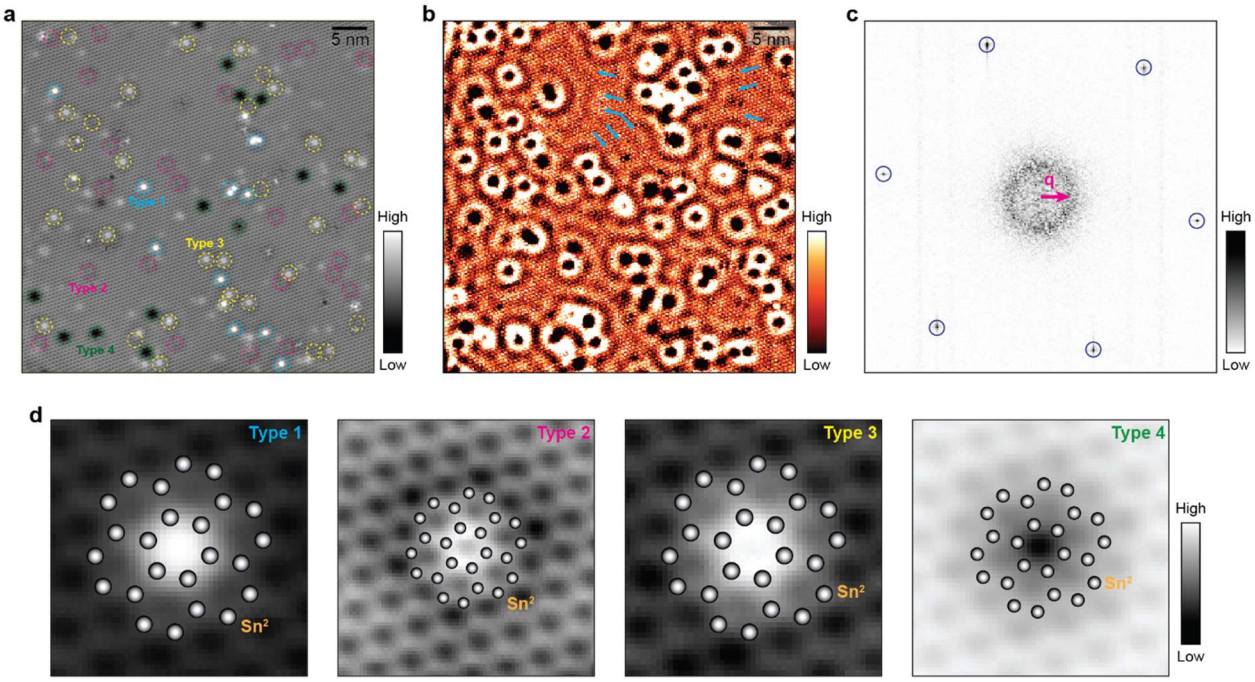

Supplementary Figure 5. Atomic-scale origins of electron scattering and interference. (a) A 50 nm square topograph of the Sn^2 surface, and (b) a dI/dV map taken in the identical region. We identify at least 4 types of impurities that give rise to notable quasiparticle interference in (b). We locate these impurities by marking all dark spots where electronic ripples originate in (b), and superimpose them on top of the topograph in (a). The impurities are denoted as type 1 (cyan circles), type 2 (magenta circles), type 3 (yellow circles) and type 4 (green circles). It can be seen that electronic waves propagates away from the impurities; select few examples are pointed out by blue arrows in (b). (c) Fourier Transform of (b), showing ring-shaped scattering wave vector **q**. Atomic Bragg peaks are circled in blue. (d) High spatial resolution topographs of the four types of impurities with Sn^2 ball model superimposed on top. The relative position between the impurity center and the ball model show that the four types could be Sn^1 or Tb vacancies or substitutions. STM setup conditions: I_{set} = 1 nA, V_{sample} = 300 mV, V_{exc} = 2 mV.

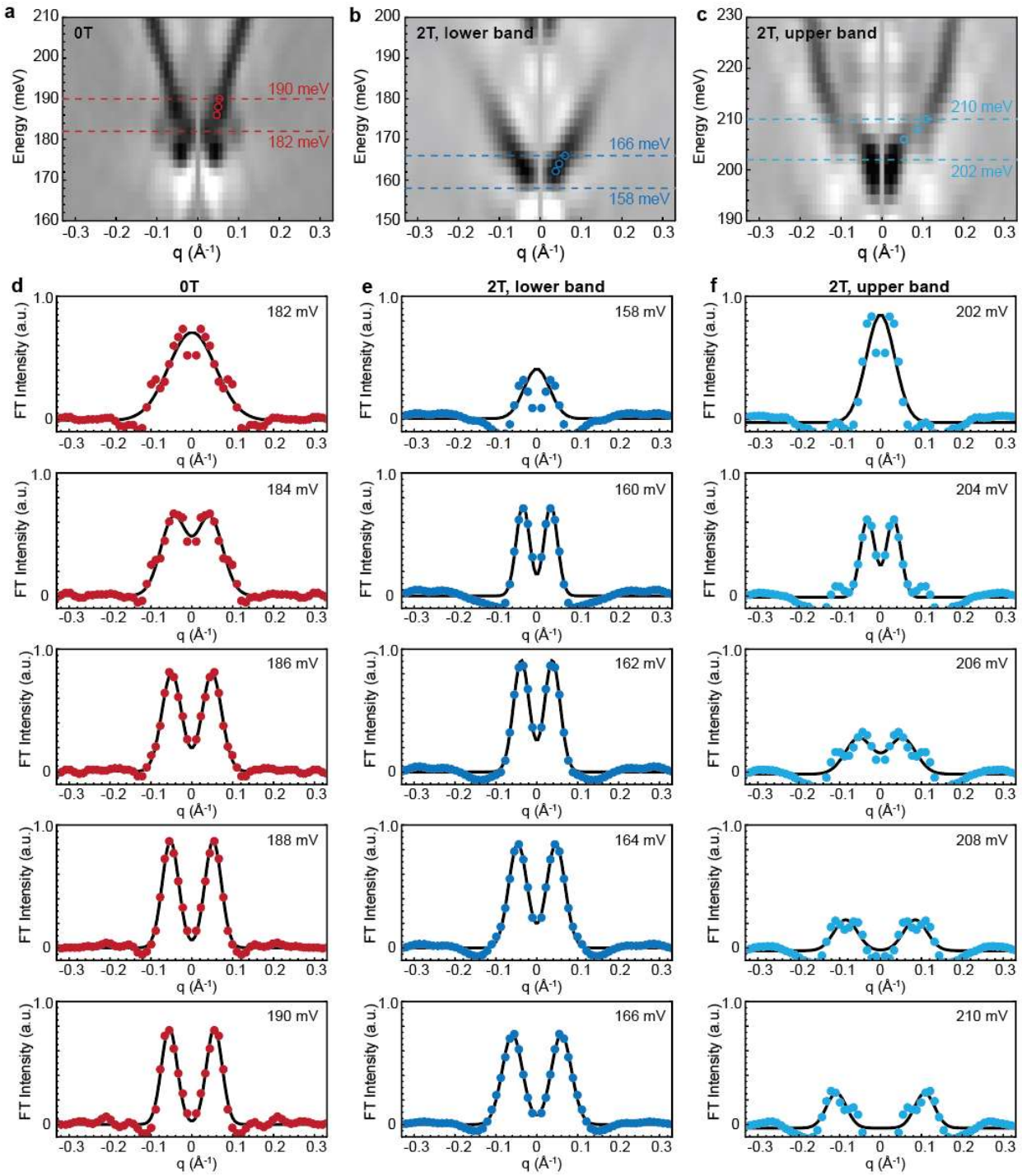

Supplementary Figure 6. More details on band fitting for small wave vectors q. (a-c) The second derivative of radially averaged FT linecuts starting at the center of the FT for (a) Dirac band at 0T, (b) lower Dirac band at 2T and (c) upper Dirac band at 2T. (d-f) Horizontal cuts obtained from (a-c) in the energy range denoted by dashed lines in (a-c). Solid circles in (d-f) are the experimental data, and solid lines represent Gaussian fits. Data points plotted in (a-c) are only those where the two peaks in the FT linecuts in (d-f) can be clearly separated from the FT center.